

See discussions, stats, and author profiles for this publication at: <https://www.researchgate.net/publication/321494371>

Mechanical response of two polyimides through coarse grained molecular dynamics simulations

Article in *Modelling and Simulation in Materials Science and Engineering* · December 2017
DOI: 10.1088/1361-651X/aa9ee4

CITATIONS
0

READS
58

8 authors, including:



Sudarkodi Venkatesan
Indian Institute of Technology Kanpur
5 PUBLICATIONS 16 CITATIONS

SEE PROFILE



Sumit Basu
Indian Institute of Technology Kanpur
76 PUBLICATIONS 704 CITATIONS

SEE PROFILE



Priya V. Parandekar
The Boeing Company
18 PUBLICATIONS 481 CITATIONS

SEE PROFILE

Some of the authors of this publication are also working on these related projects:



Mechanics of polymers [View project](#)



nanocomposites [View project](#)

Mechanical response of two polyimides through coarse grained molecular dynamics simulations

V Sudarkodi², K Sooraj¹, Nisanth N Nair¹, Sumit Basu²

Priya V Parandekar³, Nishant K Sinha³, Om Prakash³, Tom Tsotsis⁴

1. Department of Chemistry and 2. Department of Mechanical Engineering,

Indian Institute of Technology Kanpur

Kanpur 208016, UP, INDIA.

3. Boeing Research and Technology, India-Centre, Bangalore-560016, INDIA

4. Boeing Research and Technology, Huntington Beach, CA-92647, USA.

Abstract

Coarse grained molecular dynamics (MD) simulations allow us to predict mechanical responses of polymers, starting with merely a description of their molecular architectures. It is interesting to ask if, given two competing molecular architectures, coarse grained MD simulations can predict the differences that can be expected between their mechanical responses. We have studied two crosslinked polyimides PMR15 and HFPE52 — both used in high temperature applications — to assess whether subtle differences in their uniaxial stress strain responses revealed by experiments, can be reproduced by carefully coarse grained MD models. Coarse graining procedure for PMR15 is outlined in this work while the coarse grain forcefields for HFPE52 are borrowed from an earlier work [38]. We show that stress strain responses of both these polyimides are qualitatively reproduced and important insights into their deformation and failure mechanisms are obtained. More importantly, the differences in the

molecular architecture between the polyimides carries over to differences in stress strain responses in a manner that parallels experimental results. A critical assessment of the successes and shortcomings of predicting mechanical responses through coarse grained MD simulations has been made.

1 Introduction

Molecular dynamics (MD) simulations of polymers have provided insights into correlations between the molecular architecture of these synthetic materials and a range of their mechanical properties. Simulations with a view to elucidate mechanical properties have been reported for entangled long chained polymers (eg. [1]-[7]) as well as crosslinked ones (eg. for crosslinked epoxies by [8]). These studies have greatly enriched our knowledge about mechanisms which cause polymers to deform and fail. It is in fact, well established that the qualitative nature of the uniaxial stress strain responses of many polymers are well captured by molecular simulations. However, given the very large and unrealistic rate of loading that needs to be applied in these simulations, scaling of quantities like yield stress, failure strain etc. to experimentally accessible loading rates are difficult (see, [9] for a recent attempt at scaling the mechanical properties of polycarbonate, a long chained molecule).

However, even if we choose to leave the question of scaling aside, the long term technological benefits of conducting these large and expensive simulations still need to be established firmly. For instance, one may ask whether MD simulations can give us an inkling, if not a firm idea, about the differences in mechanical properties that we can expect between two competing molecular architectures. Can we use MD simulations to assess whether an intended change in architecture is going to reduce or increase a macroscopic property like the yield stress or fracture toughness? If it can, newly designed architectures can then be run through MD simulations to determine whether they are better or worse compared to similar earlier architectures. A more exciting possibility is that we may be able, using MD as a tool, to design architectures that lead to a set of targeted mechanical properties.

To critically examine the above question, we chose to perform coarse grained MD simulations on two similar polyimides. Polyimides are an important class of high temperature polymers with a wide range of applications. Homopolyimides exhibit good thermal and mechanical properties but are difficult to process with conventional polymer processing methods. The quest for improved processability has led to the development of copolymers, addition polyimides, polymerisation of monomer reactant (PMR) formulations and thermosetting polyimides. Apart from these, composites with polyimide matrix and blends of polyimides with other polymers have significantly extended their usability. These developments have led to the widespread application of polyimides in diverse fields like electrical, medical, aerospace, membrane technology and automobiles [10–12].

The polyimides that we have chosen are two crosslinked polymers of similar structure—namely, PMR15 and HFPE52. Both are crosslinked polyimides, used commercially in high temperature applications. Both PMR15 and HFPE52 are thermosetting polyimides characterised by high glass transition temperatures (T_g) of 316 and 345 °C respectively. The processing of PMR15 (historically the first commercially synthesised polyimide) entails mixing the monomers monomethylester of 5-norbornene-2, 3-dicarboxylic acid (NE), dimethyl ester of 3,3',4,4'-benzophenone tetracarboxylic acid (BTDE), and 4,4'-methylene-dianiline (MDA) in the ratio NE:BTDE:MDA of 2:2.084:3.084 so as to result in a final molecular weight of 1500. The PMR15 molecule with the nadic endcaps is shown in Fig. 1(a). On the other hand, HFPE52 is synthesised with phenylethyne (PETI) as endcap, dimethyl ester of 4,4' Hexafluoroisofropylidene-Bis Phthalic acid (HFDE) and P-Phenylenediamine (PPDA) in the ratio 5:6 ([37]). The structure of the HFPE52 oligomer is shown in Fig. 1(b).

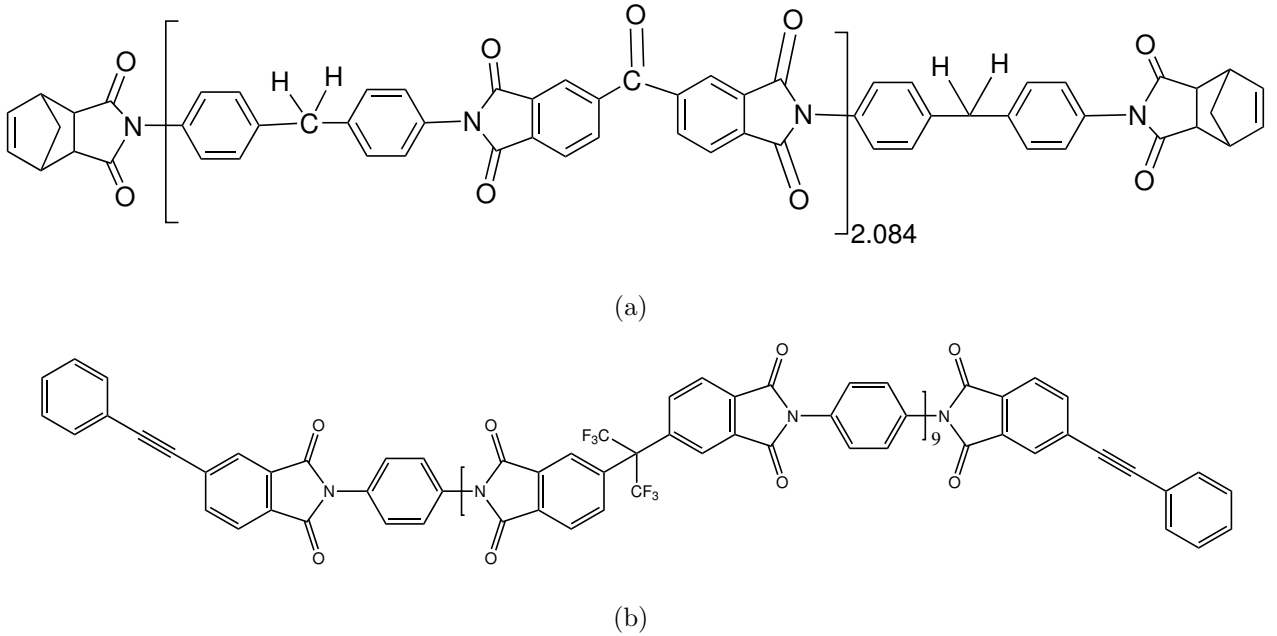


Figure 1: The (a) PMR15 and (b) HFPE52 molecules

The mechanical behaviour of PMR15 and its composites is particularly well characterised [21–24], while recently, experimental results on HFPE52 have also been reported [40]. Particularly, the stress strain curves of the two polyimides that have been characterised, among others, by [23] and [40] throw up subtle differences. The experimentally obtained uniaxial tensile responses for PMR15 at strain rates ranging between $10^{-6} - 10^{-3} \text{ s}^{-1}$ and for HFPE52 at 10^{-3} s^{-1} are shown in Figs. 2(a) and (b) respectively. Both the polyimides are relatively brittle with low yield stress. At $\dot{\epsilon} = 10^{-3} \text{ s}^{-1}$, both have a comparable yield stress of around 35 – 45 MPa, the stress carrying capacity of HFPE52 being somewhat lower than PMR15. However, HFPE52 exhibits a marked drop in stress carrying capacity right after yield, followed by an almost perfect plastic behaviour. On the contrary, PMR15 hardens monotonically after yield (though the slope of the hardening part seems to decrease with loading rate) and shows no drop in stress carrying capacity. Drop in stress carrying capacity after yield is

also exhibited by many long chained polymers and is known to cause severe localisation of strain in the material at regions of stress concentration [25]. We will examine whether MD simulations can capture the difference in uniaxial stress strain behaviour of PMR15 and HFPE52.

Attempts to reproduce experimentally observed mechanical and thermal behaviour of polyimides with detailed all-atom MD simulations have recently been reported, albeit for a different long-chained system (see, [13, 14]). Firstly, these studies highlight that preparing an equilibrated sample of these all-atom polyimide system is a difficult exercise. Several cycles of pressurisation and depressurisation at very high temperatures, followed by annealing and cooling to room temperature for a few microseconds is required to achieve a well prepared sample. Secondly, these studies have brought out the important role of electrostatic interactions in determining both uniaxial stress strain response and thermal properties like coefficient of thermal expansion and glass transition temperature in these polymers with highly polar groups. As a result, the parametrisation of the partial charges on every atom assumes importance.

The MD simulations that we have conducted are based on coarse grained forcefields. Simulations on fully detailed atomistic models of PMR15 are prohibitive for a number of reasons, most importantly from the point of view of computational costs. Extending MD simulations to longer time and larger length scales with currently available computational power requires an effective strategy for coarse graining (CG) the detailed all-atom model in order to retain only the most essential details. In the process, bringing out subtle differences in macroscopic mechanical response, in spite of jettisoning a substantial amount of information from all-atom models, becomes far more challenging.

Examples of such attempts to coarse grain particular systems include those by [15, 27–32]. The literature on coarse graining of polyimides is sparse. A CG model for a piezoelectric polyimide copolymer has been reported by [33]. Closer to our interest is the coarse grained study of HFPE30 by [38]. We have adopted the CG forcefield developed by these authors to model HFPE52. The CG model for PMR15, on the other hand, is developed as part of the present work.

We show that a systematic CG model is indeed capable of bringing out many of the experimentally observed differences in the two polyimides. Coarse grained MD simulations of the uniaxial stress strain behaviour of both polyimides lead to qualitatively realistic (but, as is usual for MD simulations at high rates of loading, quantitatively elevated) responses. Moreover, important information about the failure mechanisms operating during deformation are also obtained from these simulations.

To summarise, the focussed aim of this work is to assess whether:

- (i) standard coarse-graining techniques applied to crosslinked polyimides (with PMR15 and HFPE52 as examples) are useful for obtaining qualitative nature of their uniaxial stress-strain responses, and,

- (ii) in spite of the fact that a coarse graining procedure necessarily jettisons a lot of molecular level detail, MD simulations performed with coarse grained models can still bring out subtle differences in stress-strain responses of two related but architecturally different polyimides.

The rest of the paper is organised as follows. In the next section, the coarse graining procedure for PMR15 is described. As mentioned earlier, the coarse grained model for HFPE52 is borrowed from [38], where a number of coarse grained models for HFPE30 were discussed. The more common HFPE52 differs from HFPE30 in the number of repeating units — while HFPE30 has 5 repeating units, HFPE52 has 9. We have used the 8 bead CG model for HFPE30 to create CG-HFPE52. The essential details are discussed briefly. In Sec. 3, we present the uniaxial tensile responses with coarse grained models of PMR15 and HFPE52, compare them with experiments and discuss the insights they offer. Finally, the salient lessons learnt from this work are outlined in Sec. 5.

2 Coarse grained forcefields for polyimides

2.1 Coarse graining PMR15

A coarse grained forcefield for PMR15 has been developed systematically. The strategy adopted here is to reduce an all-atom oligomer of PMR15 (with nadic endcaps) into a coarse grained one with three beads E, M and B as shown in Fig. 3.

The procedure follows [27] and entails the following broad steps:

- (i) Determination of the optimised, minimum energy all-atom structure of PMR15 from *ab initio* computations. This exercise yields equilibrium values of all bond lengths, angles and dihedrals as well as charges on each atom. This is described in Sec. 2.1.1.
- (ii) Starting from the equilibrium structure and keeping all other degrees of freedom fixed, each dihedral is rotated in small steps (of about 10°) through 360° and the change in energy with dihedral angle is plotted.
- (iii) Dihedrals with relatively low barriers to rotation are identified. Monte Carlo simulations are now performed over these dihedrals to determine the probability distributions of the coarse grained bond lengths, angles and dihedrals. This process is described in Sec. 2.1.2.
- (iv) Boltzmann inversion is used to determine the coarse grained bonded forcefield. This is also discussed in Sec. 2.1.2.
- (v) The non-bonded forcefield is assumed to be of the Lennard-Jones (LJ) type and the parameters are determined by an ‘energy matching’ technique described in Sec. 2.1.3.

- (vi) A crosslinking strategy that mimics an established crosslinking mechanism is used to create a coarse grained sample with requisite crosslink density. This is described in Sec. 2.1.4.

2.1.1 Optimised structure of PMR15

A molecule of PMR15 has 169 atoms. In the following discussion, an ‘all-atom’ model will imply one with all the 169 atoms included. The optimized all-atom structure of PMR15 (shown in Fig. A.1) as well as all other results from *ab initio* calculations were obtained from density functional theory (DFT) based computations performed using Gaussian 09 program package [17]. B3LYP functional [18, 19] and 6-31G(d,p) basis set were used in these computations. The numbering scheme used for the PMR15 molecule has been given in Fig. A.1 in Appendix A. Further, Tables A.1, A.2 and A.3 lists the values of all bond lengths, angles and dihedrals in the optimised oligomer.

We have divided the all-atom structure of PMR15 into 3 distinct beads as shown in Fig. 3. The bead E incorporates the entire nadic endcap. The methylene dianiline and the 3', 4, 4' benzophenone tetracarboxylic acid are incorporated in beads M and B respectively. Optimised all-atom structures of the beads E, M and B (after capping them with hydrogens) have also been obtained in a manner similar to the entire PMR15 molecule. The structure, mass, charge and effective radii (i.e. the radius of the smallest sphere that encloses a bead entirely) is taken to the of the beads E, M and B are listed in Table 1. A CG-PMR15 model is constituted of seven beads of the type E, M and B.

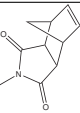
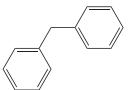
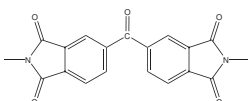
CG Bead	Structure	Mass	Charge	Radius (Å)
<i>E</i>		154	-0.22	5.6
<i>M</i>		156	0.44	6.4
<i>B</i>		312	-0.44	11.6

Table 1: Details of the CG beads in CG-PMR15

In addition to the optimised structure, barriers to torsion of all dihedrals in the all atom model were also determined. The shape of the barrier for a dihedral angle was determined keeping all other degrees of freedom frozen at their optimised values and varying the dihedral angle in question in steps of 10°, with the zero corresponding to the optimised position.

In particular, three torsion potentials (18 – 20 – 21 – 22, 24 – 25 – 26 – 27 and 28 – 29 – 44 – 45) obtained by this method are shown in Figs. 4(a) through (c). These dihedrals have relatively low barriers to rotations, (barrier heights are 25, 12 and 35 kJ/mol respectively) while all others have

much higher barriers. Thus, in the process of coarse graining, all bond lengths, angles and dihedrals *except these three* are assumed to remain fixed at their optimised values. Note that kT at 288° C is ~ 5 kJ/mol.

2.1.2 Bonded interactions in CG-PMR15

The internal degrees of freedom within a bead are sacrificed in the CG model. So, in order to be useful, the CG model, containing much fewer degrees of freedom, should be able to predict macroscopic properties faithfully. If it does, it will mean that the degrees of freedom which were sacrificed have little or no bearing on the macroscopic property in question. In our case, the macroscopic response of interest is the uniaxial stress-strain response of the polyimide. In this section, we describe the coarse graining procedure adopted for PMR15.

In the following discussions, physical quantities pertaining to the all atom model are denoted by smallcase roman letters (eg. r_{ij} for distance between atoms i and j) with atom numbers denoted by smallcase Roman subscripts. Upper case Romans are used for quantities pertaining to the CG system with uppercase subscripts and Greek superscripts denoting atom numbers (eg. R_{IJ}).

The statistics for the CG model is determined from an isolated all-atom chain (in a procedure that closely follows [27]). Intra-chain interactions along the all-atom PMR15 are taken into account but longer range non-bonded interactions are not considered. As mentioned earlier, only three dihedrals are identified as relatively mobile and can attain non-optimal values while all other bond lengths, angles and dihedrals remain unchanged at their values in an optimised isolated all-atom molecule.

The CG bonded force field is now determined by the following steps:

1. Several realisations of the all-atom PMR15 molecule, using the Metropolis Monte Carlo algorithm, with the torsion potentials $U(\phi_i)$ (where ϕ_i is one of the three dihedrals that we have identified) are generated at a chosen temperature $T = 300$ K. The method involves randomly choosing a value of the dihedral ϕ_i , reading off $U(\phi_i)$ from the determined potentials and calculating a probability $\sim \exp(-U(\phi_i)/k_B T)$ (where k_B is the Boltzmann's constant). Finally, the configuration is accepted if the probability is greater than a random number generated from a normal distribution.
2. The positions of the geometrical centers of the beads E , M and B are retrieved from each accepted realisation. Distances between the beads R_{IJ} , angles Θ_{IJK} and dihedrals Φ_{IJKL} (where I, J, K, L can be E, M or B) are determined.
3. The distribution functions $P'_s(R_{IJ})$, $P'_b(\Theta_{IJK})$ and $P'_d(\Phi_{IJKL})$ for the CG bond lengths, angles and dihedrals respectively are obtained by plotting histograms corresponding to the bond lengths between $E - M$, $B - M$ and $M - E$ (R_{EM}, R_{BM} and R_{ME}), angles between $E - M - B$,

$M-B-M$, $B-M-B$ and $B-M-E$ (Θ_{EMB} , Θ_{MBM} and Θ_{BME}) and dihedrals $E-M-B-M$ and $M-B-M-B$ (Φ_{EMBM} and Φ_{MBMB}).

4. The scaled probability distributions are obtained from $P'_s(R_{IJ})$, $P'_b(\Theta_{IJK})$ and $P'_d(\Phi_{IJKL})$ as,

$$\begin{aligned} P_s(R_{IJ}) &\propto \frac{P'_s(R_{IJ})}{R_{IJ}^2}, \\ P_b(\Theta_{IJK}) &\propto \frac{P'_b(\Theta_{IJK})}{\sin \Theta_{IJK}}, \\ P_d(\Phi_{IJKL}) &\propto P'_d(\Phi_{IJKL}). \end{aligned}$$

5. Following [27] it is assumed that the coarse-grained probability distributions factorise i.e.

$$P(R_{IJ}, \Theta_{IJKL}, \Phi_{IJKL}) = P_s(R_{IJ})P_b(\Theta_{IJK})P_d(\Phi_{IJKL}), \quad (1)$$

for any choice of I, J, K and L . This assumption allows us to write the coarse grained potentials by Boltzmann inversion as

$$\begin{aligned} U_s(R_{IJ}) &= -k_B T \ln P_s(R_{IJ}) \\ U_b(\Theta_{IJK}) &= -k_B T \ln P_b(\Theta_{IJK}) \\ U_d(\Phi_{IJKL}) &= -k_B T \ln P_d(\Phi_{IJKL}). \end{aligned}$$

Three typical coarse grained potentials obtained using the above procedure is shown in Fig. 5. The dashed lines in these plots are obtained using standard potential functions that are readily available in most MD codes. The list of the forms of and fitted parameters for standard potential functions used to describe each bonded interaction in CG-PMR15 is given in Table. 2.

It should be mentioned here that instead of fitting standard functions, tabulated potentials can also be used for each and every bond, angle and dihedral in the CG system. Gradients of these tabulated potentials however, even when approximated by splines, can be noisy and unreliable. More importantly, PMR15 turns out to be a relatively rigid molecule. Both the CG bonds, $E-M$ and $M-B$ have very narrow distributions around the equilibrium values of 7.03 and 10.55 Å respectively. Similarly, all CG angles except $M-B-M$ also have very narrow distributions about their equilibrium values. The angle $M-B-M$ has been fitted with a quartic potential that has four undetermined parameters (as against two in a harmonic potential). Both the dihedral distributions $E-M-B-M$ and $M-B-M-B$ turn out to be almost identical and could be fitted well with the function shown in Table 2.

2.1.3 Non-bonded potentials for CG-PMR15

Proper calibration of non-bonded interactions between the beads is essential for predicting mechanical properties of a solid. A heuristic method seems to work well in this case and is described here. Our

Bond	Force field type	Equation	Parameters
Stretching			
$E - M$	Harmonic	$U_s(R) = K_s(R - R_0)^2$	$K_s = 48.26 \text{ kJ/mol } \overset{\circ}{\text{\AA}}^2$, $R_0 = 7.03 \text{ } \overset{\circ}{\text{\AA}}$
$M - B$	Harmonic	$U_s(R) = K_s(R - R_0)^2$	$K_s = 48.26 \text{ kJ/mol } \overset{\circ}{\text{\AA}}^2$, $R_0 = 10.55 \text{ } \overset{\circ}{\text{\AA}}$
Bending			
$E - M - B$	Harmonic	$U_b(\Theta) = K_b(\Theta - \Theta_0)^2$	$K_b = 0.068 \text{ kJ/mol}$, $\Theta_0 = 130.73^\circ$
$B - M - B$	Harmonic	$U_b(\Theta) = K_b(\Theta - \Theta_0)^2$	$K_b = 0.13 \text{ kJ/mol}$, $\Theta_0 = 126.92^\circ$
$M - B - M$	Harmonic	$U_b(\Theta) = K_b(\Theta - \Theta_0)^2$	$K_b = 0.13 \text{ kJ/mol}$, $\Theta_0 = 171.26^\circ$
Dihedral			
$E - M - B - M$, $M - B - M - B$	Cosine	$U_d(\Phi) = K_d[1 + d \cos(n\Phi)]$	$K_d = 3.85 \text{ kJ/mol}$, $d = -1$, $n = 0.017$

Table 2: Standard potential functions and parameters used to approximate the Boltzmann inverted bonded potentials in CG-PMR15.

method of calibrating non-bonded CG potentials may be called an ‘energy matching technique’. This is similar in spirit to the ‘force matching technique’ adopted by [32] and [15] where a spline based force field is fitted such that forces on beads match that on the group of atoms making up the bead. On the other hand, our method is unlike that due to Faller and co-workers ([31], [34]) where the force field parameters are iteratively refined in order to accurately match the non-bonded radial distribution functions (rdf).

A small all-atom sample of PMR15 (containing 125 molecules, each with 169 atoms) is equilibrated at $T = 298 \text{ K}$ and 1 MPa pressure under an NPT ensemble in the commercial MD software Materials Studio using the PCFF forcefield. Post equilibration, a production run was conducted at the same temperature and pressure for 50000 ps with a time step of 1 fs. The ensemble settled down to a density of 1300 kg/m^3 , which is close to the experimental density of PMR15.

The non bonded potentials between all pairs of beads are taken to be of the Lenard Jones (LJ) type. To facilitate the discussion, the beads E, M and B will be represented by Greek alphabets. Let i_α denote an atom in the detailed atomistic ensemble that is mapped onto species α . Also let n_α denote the number of atoms that constitute the CG species α , i.e. $i_\alpha \in [1, n_\alpha]$. Also I_α is a CG bead of species α . Thus, the position vector for the centre of the bead is:

$$\mathbf{R}_{I_\alpha} = \frac{1}{n_\alpha} \sum_{i_\alpha=1}^{n_\alpha} \mathbf{r}_{i_\alpha}, \quad (2)$$

where \mathbf{R}_{I_α} and \mathbf{r}_{i_α} are the position vectors of the bead I_α and atom i_α respectively.

In the present case, 6 non-bonded interactions $U_{\alpha\beta}$ need to be determined between the beads E ,

M and B . These are determined using,

$$U_{\alpha\beta}(R_{I_\alpha I_\beta}) = \sum_{i_\alpha=1}^{n_\alpha} \sum_{i_\beta=1}^{n_\beta} \phi_{i_\alpha i_\beta}(r_{i_\alpha i_\beta}), \quad (3)$$

where $R_{I_\alpha I_\beta} = |\mathbf{R}_{I_\beta} - \mathbf{R}_{I_\alpha}|$ and $r_{i_\alpha i_\beta} = |\mathbf{r}_{i_\beta} - \mathbf{r}_{i_\alpha}|$ and $\phi_{i_\alpha i_\beta}(r_{i_\alpha i_\beta})$ denotes the non-bonded potential between atoms $i_\alpha \in \alpha$ and $i_\beta \in \beta$.

From the all-atom production run at 298 K, several I_α, I_β pairs can be identified at different distances $R_{I_\alpha I_\beta}$ over the entire time frame for which it is run. For example, Fig. 6(c) shows U_{BB} plotted against all $R_{I_B J_B}$. Each point in the plot is an instance of a $B - B$ interaction in the sample. Also shown on this plot is a Lenard Jones (LJ) potential that fits the $U_{BB}(R_{I_B J_B})$ data reasonably well. The all atom simulations show that two B superatoms cannot come closer than 5 \AA . It should be noted that the LJ potential represents only the short range van der Waals interactions and the electrostatic interactions have to be accounted for separately. The 6 distributions of $U_{\alpha\beta}(R_{I_\alpha J_\beta})$ are shown in Figs. 6(a) through (f). In each case, the radially isotropic LJ potential is used and the parameters to be fitted are the well depth ϵ and the inter-bead distance at which the interaction is zero, σ .

The choice of a spherically symmetric LJ potential is limiting in a number of ways. The all-atom structure of the beads is not spherical and approximating them with hard sphere beads leads to fact that MD simulations of CG-PMR15 with the σ and ϵ values obtained from the fits in Fig. 6(a)-(f) do not reproduce the density of the all-atom model. Moreover, comparing the hard sphere bead radii given in Table 1 with Figs. 6(a)-(f), we see that the σ values in the fitted LJ curves are smaller than the hard sphere van der Waals radii in all the cases. For instance, for the BB interaction, the fitted value of σ is 5.0 \AA while the van der Waals radius of two hard sphere BB beads is 5.6 \AA .

In order to reproduce the all-atom density at 298 K and 1 atm pressure, we need to tinker the ϵ and σ values (the σ values should be close to and less than the van der Waals radius of the interaction in question). The values of σ and ϵ obtained from the energy matching technique only serve as an initial guess. The values obtained from the fits in Figs. 6(a)-(f), the van der Waals radii and the final values used to get the correct all-atom density are listed for all the 6 interactions in Table. 3.

Finally therefore, the LJ parameters are determined by a somewhat crude optimisation that forces the CG system to have the correct all-atom density at the given pressure. Note that, simultaneous matching of multiple physical quantities (in our case, energy and density of the ensemble at a given pressure and temperature) between all-atom and CG simulations by merely adjusting the parameters in the LJ interactions energies, is a difficult task. The problem has been widely discussed in the literature (see, [16], [15]). A direct manipulation of the non-bonded potential parameters (starting from a guess provided by the energy-matching or equivalent technique), at this time, seems to be the only viable route.

Bond	Force field type	Fitted parameters	Maximum vdW radius	Final parameters
Nonbonded				
$E - E$	LJ	$\epsilon = 14.63 \text{ kJ/mol}, \sigma = 5.0 \text{ \AA}$	5.6 \AA	$\epsilon = 4.97 \text{ kJ/mol}, \sigma = 5.0 \text{ \AA}$
$M - M$	LJ	$\epsilon = 17.55 \text{ kJ/mol}, \sigma = 3.95 \text{ \AA}$	6.6 \AA	$\epsilon = 5.14 \text{ kJ/mol}, \sigma = 5.45 \text{ \AA}$
$B - B$	LJ	$\epsilon = 46.81 \text{ kJ/mol}, \sigma = 4.5 \text{ \AA}$	11.6 \AA	$\epsilon = 12.67 \text{ kJ/mol}, \sigma = 7.2 \text{ \AA}$
$E - M$	LJ	$\epsilon = 14.63 \text{ kJ/mol}, \sigma = 4.5 \text{ \AA}$	6.1 \AA	$\epsilon = 5.14 \text{ kJ/mol}, \sigma = 5.65 \text{ \AA}$
$M - B$	LJ	$\epsilon = 29.67 \text{ kJ/mol}, \sigma = 4.2 \text{ \AA}$	9.1 \AA	$\epsilon = 11.2 \text{ kJ/mol}, \sigma = 7.1 \text{ \AA}$
$E - B$	LJ	$\epsilon = 24.24 \text{ kJ/mol}, \sigma = 4.3 \text{ \AA}$	8.6 \AA	$\epsilon = 8.78 \text{ kJ/mol}, \sigma = 6.95 \text{ \AA}$

Table 3: Lenard Jones potential ($U(r) = 4\epsilon [(\sigma/r)^6 - (\sigma/r)^{12}]$) for CG-PMR15.

With the nonbonded parameters in the last column of Table 3, static properties of the CG sample match the all-atom sample well. The densities of both samples are equal and the average end-to-end distance of the PMR15 and CG-PMR15 molecules is 41 \AA . That the structure of CG-PMR15 is closely similar to all-atom PMR15 is further demonstrated by Figs. 7(a) and (b). These plots show contours of the correlation between the dihedral angle Φ_{EMBM} and Θ_{EMB} obtained from several CG and all atom PMR15 chains. The most preferred value for the angle Θ_{EMB} is fixed at about 131° while the dihedral Φ_{EMBM} prefers values between -60° and 60° . The similarity between the two plots indicates that the CG model indeed samples the favourable configurations from the all-atom model.

It is widely known that because of smooth hard sphere beads, CG models typically exhibit faster dynamics compared to all atom ones ([35], [38]). Effects of faster dynamics are manifested in the high values of the diffusion coefficient (calculated from the averaged mean squared displacement (MSD) of the centers of mass of the chains). The diffusion coefficient from the MSD computed from the all atom PMR15 simulation is $2.7 \times 10^{-3} \text{ \AA}^2/\text{ps}$ while that from the CG-PMR15 simulation is 5 times higher. As discussed in [38], this implies that the CG-PMR15 should show a similar stress-strain response as the all-atom sample when subjected to a strain rate approximately 5 times higher.

2.1.4 Crosslinking in CG-PMR15

The major crosslinking mechanism in PMR15 (proposed by [20] and shown in Fig. 8), is the cleavage of the double bond in the nadic endcap. In other words, crosslinking occurs by cleaving the double bonds connecting atom numbers 168 and 169 or 2 and 3 in Fig. A.1. This mechanism leads to the formation of a networked structure that derives its mechanical strength from the interconnectedness.

We attempt to mimic the network formation in the CG model. By this mechanism, each molecule of CG-PMR15 in the ensemble can connect to 4 other CG-PMR15 chains, so that, the maximum number of crosslinks possible is twice the number of CG-PMR15 molecules present. The ratio of the actual number of crosslinks formed to the maximum number possible is defined as the crosslink density and denoted by χ .

The pseudocode for the crosslinking algorithm is given in Algorithm 1. By this algorithm, two nadic endcaps, represented by E beads, form a crosslink if they are within a specified distance of each other. When all such E beads are crosslinked, the system is equilibrated under an NPT ensemble. If the desired crosslink density is not attained, the specified distance is increased and the process is repeated. The mechanism in [20] is exactly mimicked when every E bead forms exactly two new bonds with similar beads in two other CG-PMR15 chains. We have been able to achieve crosslink densities upto 0.8 using the algorithm given above.

2.2 Coarse graining HFPE52

The HFPE52 molecule is shown in Fig. 1(b). In an earlier work [38], we have coarse grained the molecule HFPE30 to three different levels of detail. It has been shown in that work that, a 8 bead CG model for HFPE30 performs at par with the all-atom model of the same polymer. For instance, the glass transition temperature of both the systems, at similar rates of cooling from the melt are close to within 20 K. Compressibility is also matches within about 25% whereas for coarser models (3 bead and 4 bead CG models of HFPE30 were also compared), the difference is generally by more than an order of magnitude. Most importantly, the uniaxial stress-strain response of the 8-bead CG model for HFPE30 out-performed that of the coarser models quite comprehensively. While friction had to be added to the smooth beads (in order to compensate for the faster dynamics in the CG models) of the 3 and 4 bead CG models, in order to match the stress strain response of the all-atom case, the 8 bead CG model reproduced the uniaxial response without any modifications.

The definition of the 8 beads in CG-HFPE52 is shown in Fig. 9 for the sake of completeness. All the parameters for the bonded forcefields are given as supplementary data in [38]. Tabular forms were used for the non-bonded interactions. These forms were provided to us by the authors of [38].

The crosslinking mechanism in HFPE52 is similar to that of PMR15. The triple bond in the PETI endcap breaks to form two possible sites for crosslinking with two other HFPE52 molecules. In CG-HFPE52, the triple bond is represented by the bead B . Thus, in CG-HFPE52, crosslinking proceeds by the bead B forming bonds with at most two other beads B in different molecules. The algorithm for creating a crosslinked CG-HFPE52 sample is same as Algorithm 1 with E in CG-PMR15 replaced by B in CG-HFPE52.

Algorithm 1 Crosslinking algorithm

```
1: target  $\leftarrow$  1.0 ▷ target crosslink density is 100%
2: cutoff  $\leftarrow$  2 Å ▷ We start by looking for chain ends which are within 2 Å of each other
3: Equilibrate the sample in an NPT ensemble at the required pressure and temperature
4: num_crosslinks  $\leftarrow$  0 ▷ number of crosslinks formed in the current cycle
5: for all possible chain end pairs in two separate chains do
6:   Find the distance between the chain ends
7:   if the distance is less than cutoff then
8:     if neither chain end already has two crosslink bonds then
9:       Form a new crosslink bond
10:      Recalculate crosslink density
11:      num_crosslinks  $\leftarrow$  num_crosslinks + 1
12:    end if
13:  end if
14: end for
15: if target crosslink density has been reached then
16:   break ▷ crosslinking to the extent desired is complete
17: end if
18: if cutoff  $\geq$  max_cutoff then
19:   break ▷ maximum cutoff reached before desired level of crosslinking is achieved
20: end if
21: if num_crosslinks  $\neq$  0 then ▷ some new crosslinks have been formed in this cycle
22:   go to 3
23: else
24:   if cutoff < max_cutoff then
25:     cutoff  $\leftarrow$  cutoff + 0.1 * cutoff ▷ if no new crosslinks have been formed, increase the cutoff
26:   end if
27:   go to 4
28: end if
```

3 Uniaxial stress strain responses of CG-PMR15 and CG-HFPE52

Samples of CG-PMR15 and CG-HFPE52 were prepared, crosslinked to a density of 80 % by the scheme represented in Algorithm 1 and further equilibrated under NPT conditions to a temperature of 560 K and 1 bar pressure. After equilibration, the simulation boxes were cubes with edge lengths $L_0 = 208$ and 189 \AA for CG-PMR15 and CG-HFPE52 respectively. A total of 70000 beads were used in case of CG-PMR15 while the CG-HFPE52 sampel had 121000 beads. The essential details of the simulations with PMR15 and HFPE52 are given in Table 4. These samples were then subjected to uniaxial strain under a $N\sigma_{xx}\sigma_{yy}l_zT$ ensemble with $\sigma_{xx} = \sigma_{yy} = 0$ and the length in the z direction controlled with time t according to:

$$l_z = L_0 + v_0 t. \quad (4)$$

Here, v_0 is a constant velocity imparted to the face at $z = L_0$. The velocity is changed between runs to give different strain rates. The strain rate $\dot{\epsilon}$ is defined as v_0/L_0 . In all cases, the strain rates achieved were much higher than the experimentally realisable and ranged between 5×10^7 and $5 \times 10^9 \text{ s}^{-1}$. All MD runs reported hereafter were performed with LAMMPS [36].

Coarse grained system	No of beads	Beads/chain	Total number of beads	Initial box size (\AA)
PMR15	3	7	70000	208
HFPE52	8	25	121000	189

Table 4: Essential details of the coarse grained MD simulations conducted to simulate uniaxial response of PMR15 and HFPE52

The engineering strain component of interest is $\epsilon_{zz} = l_z/L_0 - 1$ and the corresponding stress is σ_{zz} , which we identify with the same component of the virial stress computed over the volume of the entire simulation box. Another quantity of interest is the evolution of the void volume fraction v_f with deformation. The void volume fraction in a sample is computed by simply subtracting the volume occupied by the beads from the current volume of the simulation box.

The uniaxial response of CG-PMR15 and CG-HFPE52 at the same temperature and strain rate of $5 \times 10^8 \text{ s}^{-1}$ is shown in Fig. 10(a). On comparing this with the experimental responses in Fig. 10, two important qualitative similarities become apparent, namely,

1. As in the experiments, the yield stress of CG-HFPE52 is slightly lower than that of CG-PMR15 at the same strain rate.
2. After yielding, CG-HFPE52 softens considerably while CG-PMR15 shows monotonic hardening. The hardening in CG-PMR15 is steeper than in the experiments. This is possibly due

to the fact that we do not allow crosslinks to break in the simulation. This allows for a bit of stretching of the crosslink bonds as strain increases. Stretching of bonds leads to an additional contribution to the virial stress and has been shown to cause hardening in long chained polymers under tension (see [39]). In experiments, PMR15 breaks at about 12 % strain.

That the steeper hardening in the simulations is due to stretching of the crosslink bonds can be further demonstrated by performing simulations with CG-PMR15 at different crosslink densities. In Fig. 10(b), we have shown the uniaxial response of three CG-PMR15 samples with two more crosslink densities of 60 and 10 %. Clearly, the steepness of the hardening part decreases with decrease in crosslink density. As this is not allowed to happen in case of $\chi = 0.8$, the steep hardening is observed. This indirectly shows that loss of crosslinks during deformation is responsible for the low rate of hardening seen in experiments as well as, possibly, for the low strain at failure.

3. Consequently, the almost perfectly plastic behaviour of HFPE52 after the yield drop must be due to the fact that the crosslinks in HFPE52 do not stretch much during deformation. If they did, the response from the MD simulation would have shown hardening for the same reason that it does for PMR15.

On the other hand, softening in the stress strain response (called the ‘yield drop’) is a feature observed in many long chained polymers and its reasons have been widely discussed in the literature (see, eg. [39]). Appearance of such yield drops is related to a burst of rapid void nucleation due to conformational adjustments taking place at the onset of plasticity. We have not tracked nucleation and growth of individual voids in the samples as done in [39], but have plotted the overall void volume fraction v_f in Fig. 11. The void volume fraction is defined as the ratio of the change in void volume in an ensemble and its void volume at the start of the deformation. Clearly, v_f in CG-HFPE52 is much higher and grows much faster with strain ϵ_{zz} . Note that in a $N\sigma_{xx}\sigma_{yy}l_zT$ ensemble ϵ_{xx} and ϵ_{yy} are non-zero.

We believe that being a larger and somewhat more flexible molecule, CG-HFPE52 allows more free volume to develop, especially at strains where it is close to transitioning to the plastic state. However, further investigations are needed to clearly establish this point. It should be noted that the existence of the yield drop is technologically significant. It has been shown (see, eg. [25]) that softening at the early stages of deformation leads to intense localisation of strains in narrow bands at say, tips of cracks or defects.

After the yield drop, HFPE52, again like in the experimental result of Fig. 2(b), behaves almost like an elastic-perfectly plastic material. Note that, like in the case of CG-PMR15, we have not allowed the crosslink bonds to break. But even then, unlike CG-PMR15 (see, Fig. 10 and the

discussion around it), the material does not harden after yield. This shows that the crosslinks are not stretched during plastic deformation and do not contribute to the overall virial stress. We therefore conclude that damage due to loss of crosslinks is unlikely for CG-HFPE52.

4 Conclusions

We have compared the uniaxial stress strain responses of two similar polyimides that are widely used in high temperature applications through coarse grained MD simulations. Comparisons have been made at 561 K, atmospheric pressure and high strain rates.

The coarse grained force fields for both the polymers have been carefully derived. This is a crucial step. The bonded interactions can be systematically obtained through a standard route that involves a series of *ab-initio* calculations followed by the inverse Boltzmann method. The non-bonded interactions however, are somewhat difficult to obtain satisfying the criteria that multiple physical quantities like energies, virials, rdf's and other quantities should match those from a similar all-atom model. The fitting of the CG non-bonded force field is therefore, still somewhat of a heuristic process. But fidelity of the non-bonded forcefield is crucial for getting the mechanical response right. We believe that indirect confirmation of the fidelity lies in the following observations:

- The dynamics of the 8 bead CG model for HFPE52 and the 3 bead model for PMR15, is not orders of magnitude faster than the corresponding all atom systems. Diffusion coefficients obtained from mean squared displacements of the chain centroids, are of the same order (see Table 1 in [38]) and 5 times higher than the all-atom cases for HFPE52 and PMR15 respectively.
- The average structure of the CG molecules also closely resemble that of their all-atom counterparts.
- Gross static measures like density, compressibility, elastic modulus at the simulated temperature and pressure, are close to the experimental values.

With the above checks, the uniaxial responses of HFPE52 and PMR15 from the MD simulations exhibit many of the salient differences between their uniaxial responses. We enumerate them below.

- The maximum stress carrying capacity of PMR15 is experimentally found to be about 22 % more than HFPE52 at similar rates of loading. The coarse grained MD simulations bear this out, though the yield stresses predicted are higher than the experimental.
- The uniaxial response of HFPE52 shows a prominent yield drop while PMR15 does not. The yield drop is significant as such features in other polymers are known to lead to intense strain localisation during deformation. The MD simulations are able to reproduce this difference

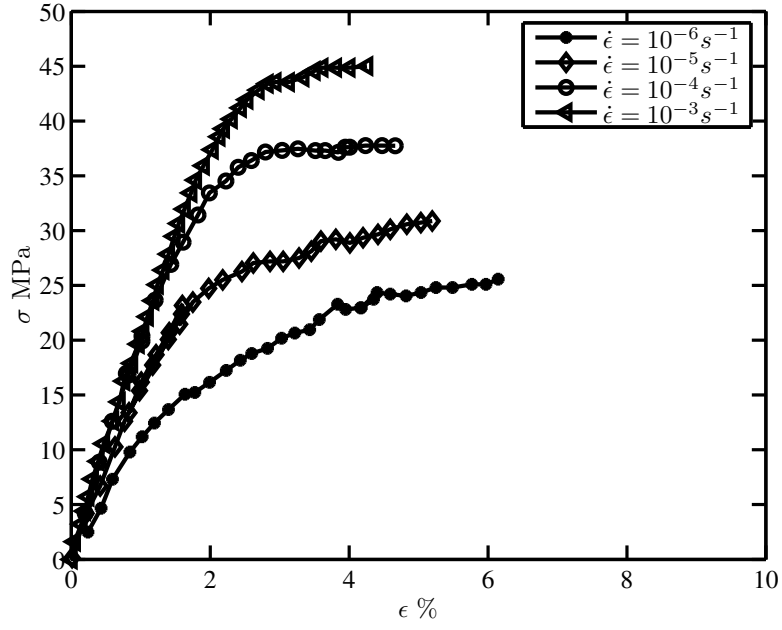
between the two polyimides. Note that the starting point of our coarse grained MD simulations are a description of the molecular architecture and crosslinking mechanism. In that sense, the fact that this subtle difference in response of the two polyimides could be reproduced by the simulations is indeed encouraging.

- The simulations have shed light on the post yield response of PMR15. It seems that the post yield response and failure at rather low levels of strain of PMR15 is marked by rapid loss of crosslinks.
- For HFPE52, the major damaging mechanism seems to be the rapid evolution of voids in the material. In fact, this seems to be the reason for the appearance of the yield drop.
- The lack of hardening in HFPE52 following the yield drop is also reproduced by the MD simulations. In fact, this points to the fact that loss of crosslinks is not a major concern for HFPE52.

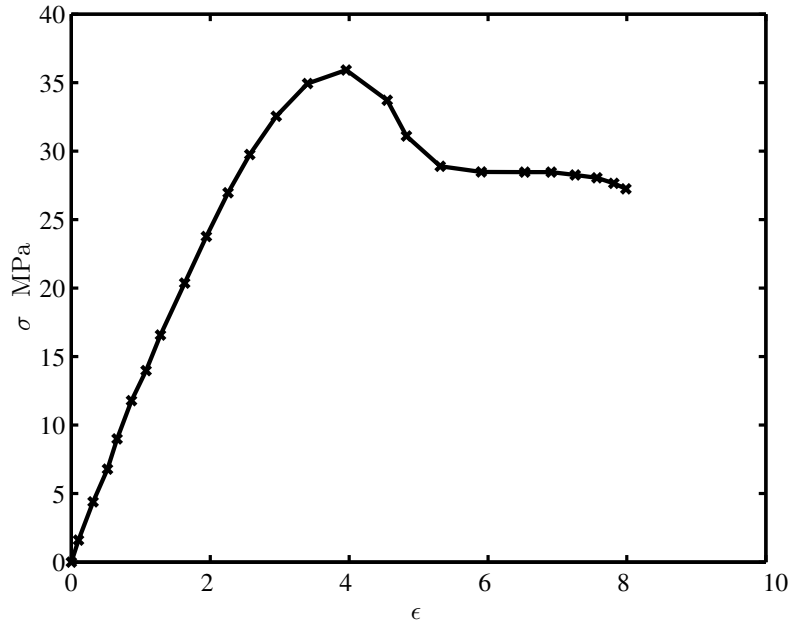
There are several aspects of the experimental stress strain responses that are not reproduced well. The peak stress in HFPE52 is attained at much higher level of strain compared to experiments where it is reached at around 4 %. Similarly, for PMR15 too, the yield strains are higher than in experiments.

Lastly, and most importantly, attempts to find a suitable scaling mechanism that may allow us to predict experimental yield stresses at strain rates of the order of, say, $1 \times 10^{-3} \text{ s}^{-1}$ from MD stress strain curves have not been successful.

We attempted to fit a overstress model [26, 41] to both the experimental and MD results of PMR15. This model, in its simplest 1-dimensional form, is analogous to a spring and viscous dashpot model (the dashpot responding to an overstress rather than the total stress, so that rate effects appear only when a threshold stress is reached) with viscosity η . For PMR15, it seemed possible to vary the viscosity with strain rate as $\eta \sim \dot{\epsilon}^{-0.975}$ to fit the the MD results. The same variation could then be used in order extrapolate to experimentally accessible strain rates. The extrapolation worked in the sense that the experimental yield stresses were predicted well by the extrapolation (i.e. changing only the viscosity and holding all other parameters to the values used to fit the MD results). However, the success of the viscosity extrapolation for PMR15 is probably fortuitous as the procedure did not work for HFPE52. A simple scaling of constitutive parameters is clearly not sufficient to predict low strain rate responses from those obtained by MD.



(a)



(b)

Figure 2: Uniaxial tensile stress strain responses of (a) PMR15 at a range of loading rates from $10^{-6} - 10^{-3} \text{ s}^{-1}$ (from [23]) and (b) HFPE52 at a loading rate of 10^{-3} s^{-1} (from [40]).

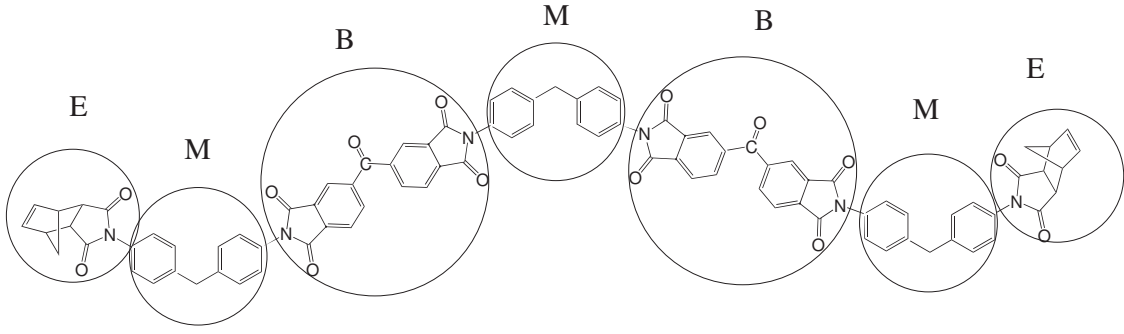


Figure 3: Definition of coarse grained beads E, M and B for the PMR15 molecule.

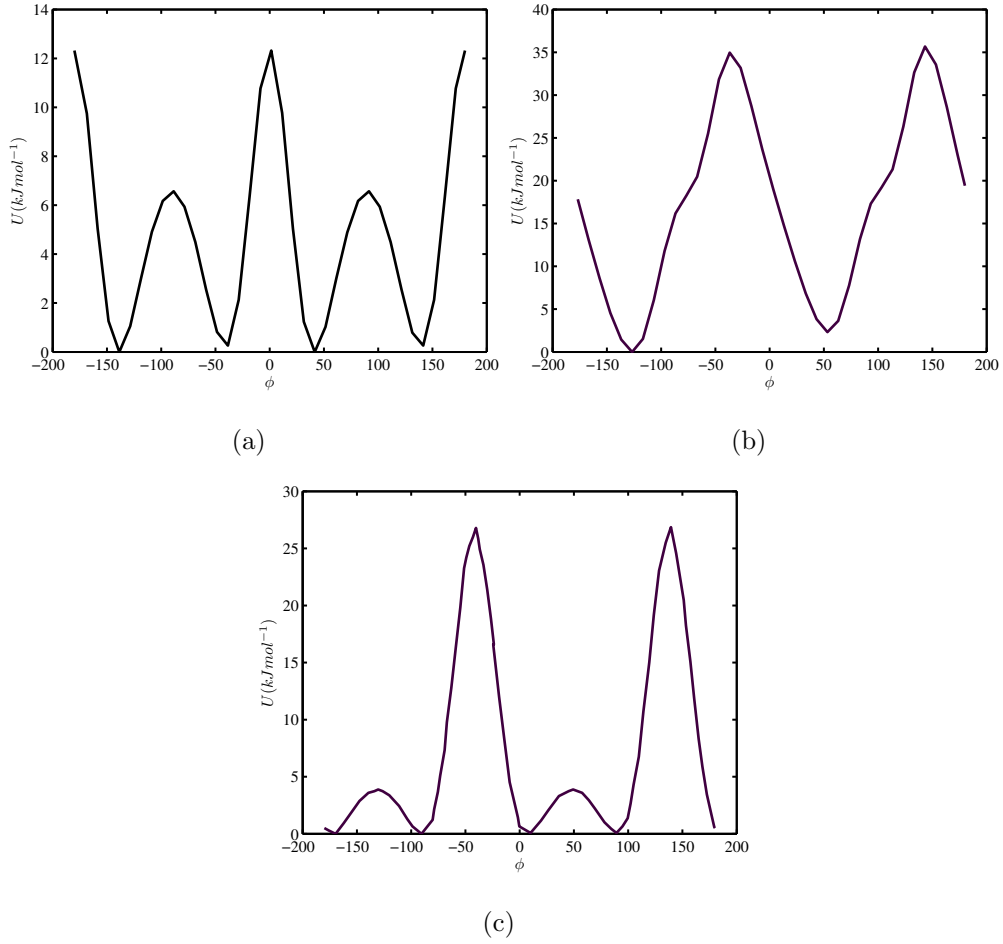


Figure 4: Torsional energy barriers for the dihedral angles (a) $\phi_{18-20-21-22}$, (b) $\phi_{24-25-26-27}$ and (c) $\phi_{28-29-44-45}$ obtained from *ab-initio* calculations.

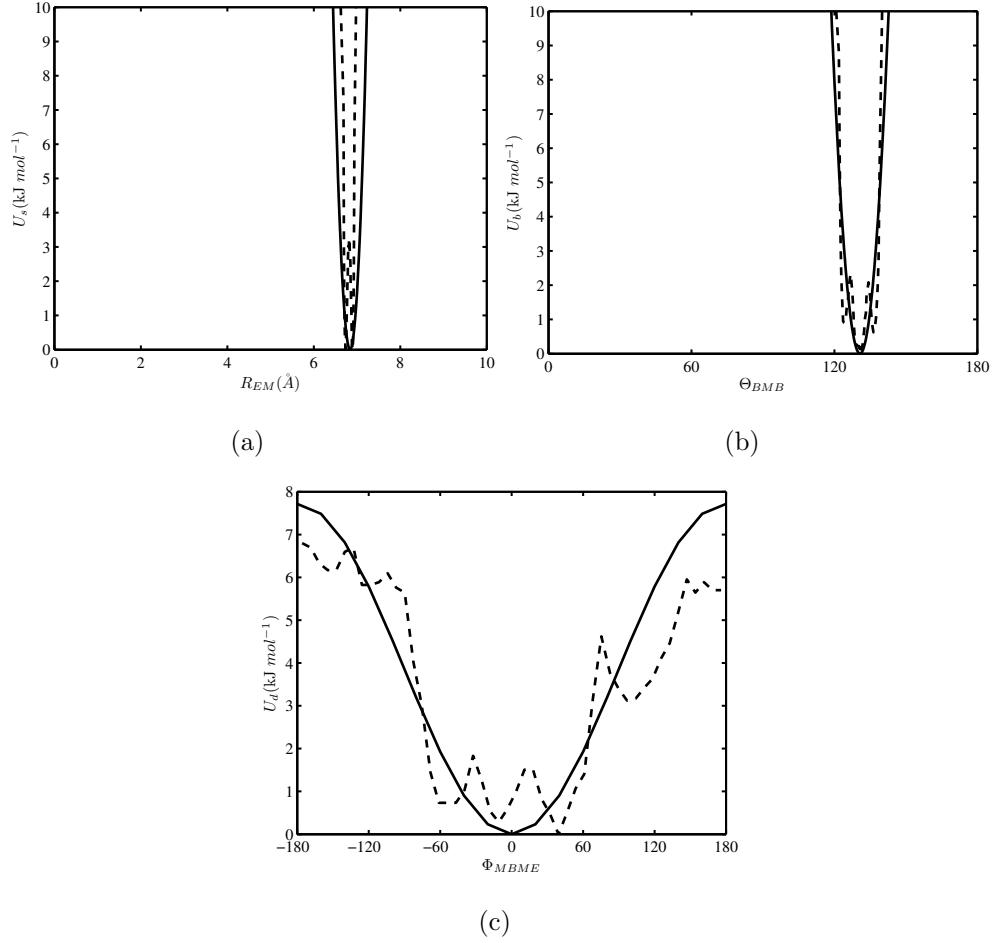


Figure 5: Boltzmann inverted potentials obtained for a representative (a) bond (E-M), (b) angle (B-M-B) and (c) dihedral (M-B-M-E) for the CG-PMR15 molecule. The dashed lines are approximations to the inverted potentials, made using standard potential functions. The functions are listed in Table 2.

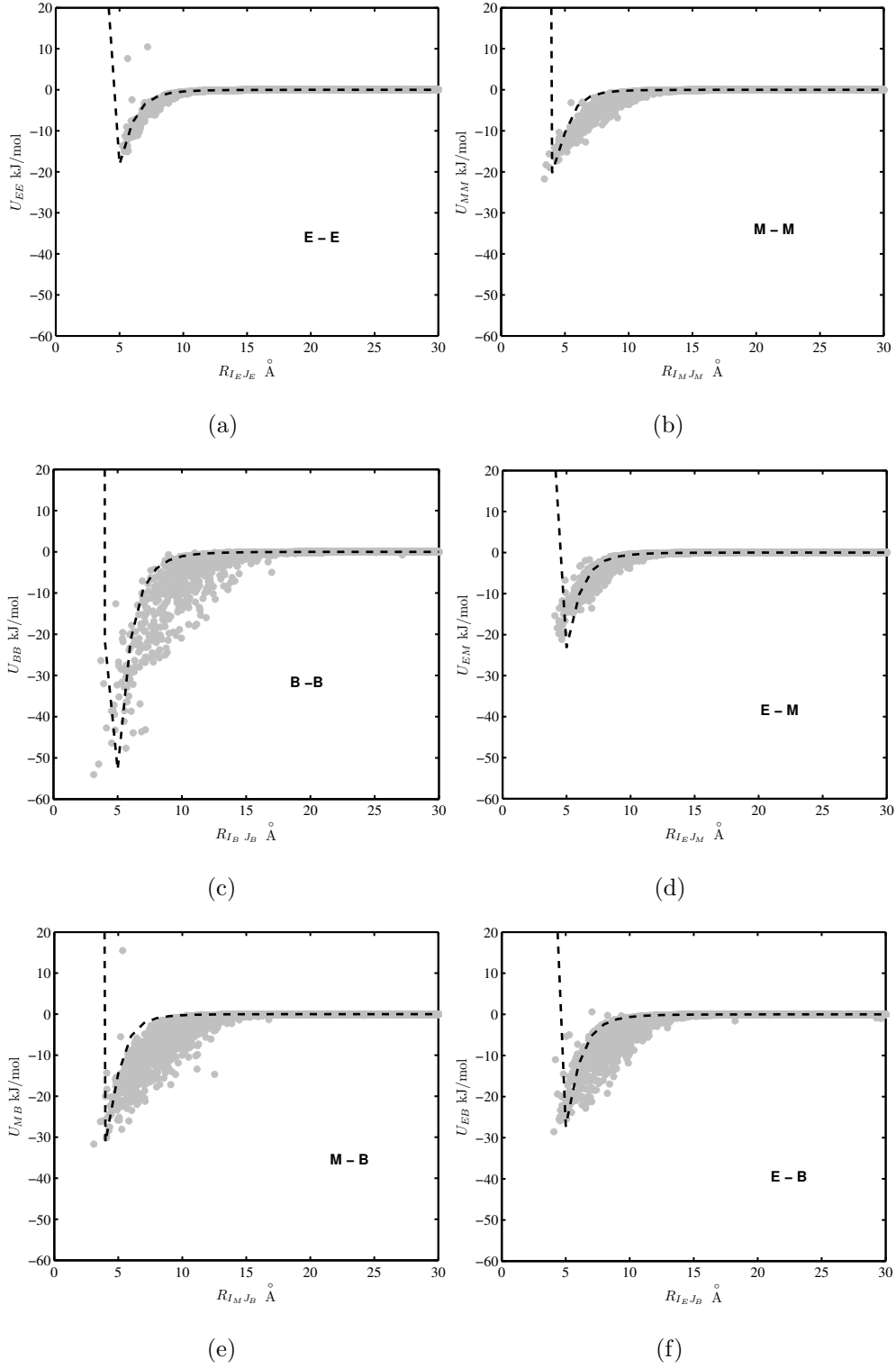


Figure 6: Variations of the non bonded energy with the distance between a species pair for α and β (a) E,E, (b) M,M, (c) B,B, (d) E,M, (e) M,B and (f) E,B respectively. The dotted lines indicate approximations to the energy with LJ potentials. The parameters used to fit the LJ potentials are listed in Table 3.

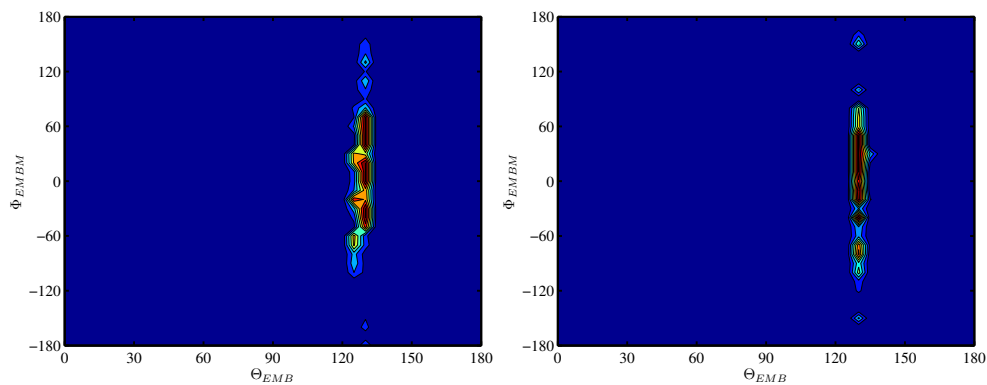


Figure 7: Contours of cross correlation between the angle Θ_{EMB} and dihedral Φ_{EMBM} obtained from all atom PMR15 and CG-PMR15 chains.

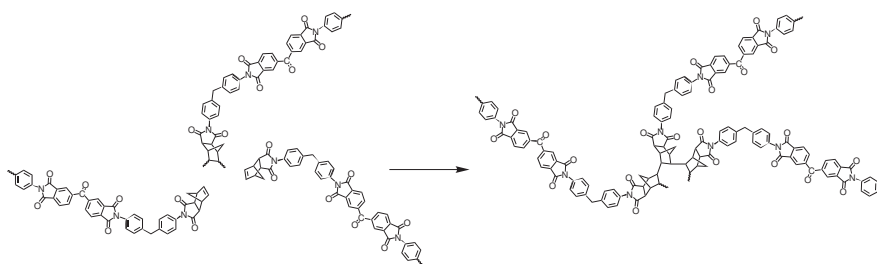


Figure 8: The major crosslinking mechanism for PMR15 according to [20]. The mechanism involves cleaving of the double bond at the end of the nadic endcap.

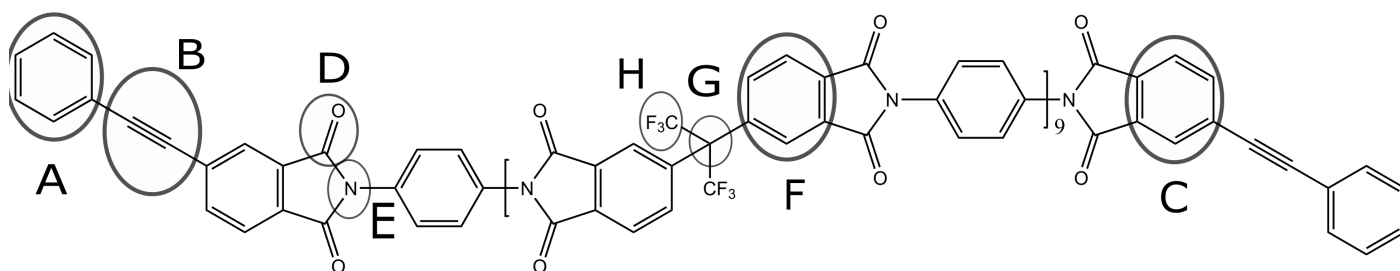
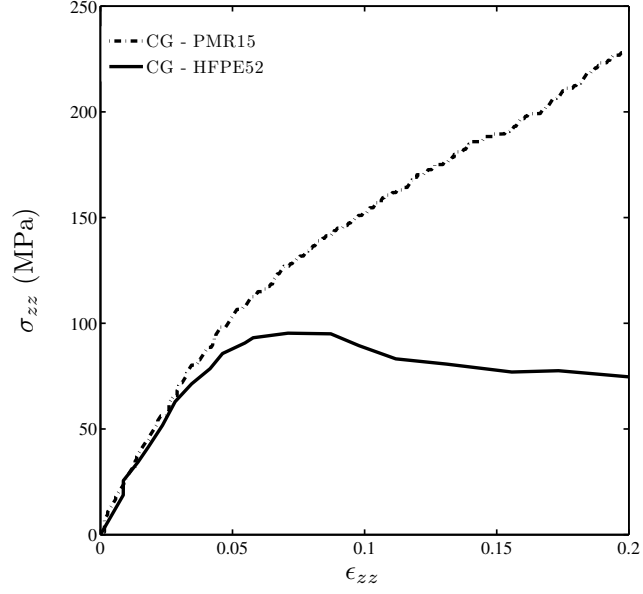
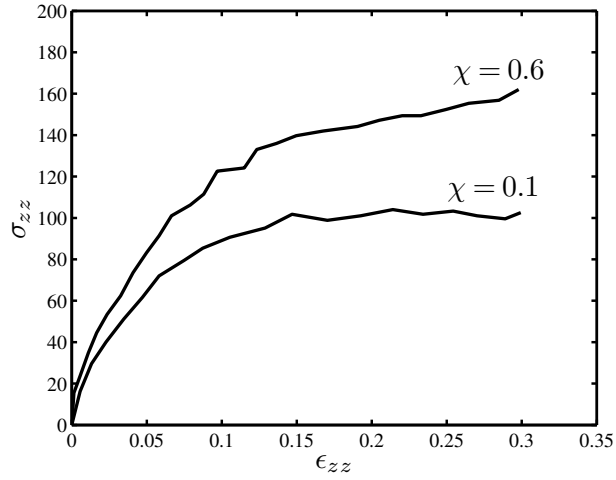


Figure 9: Definition of coarse grained beads A to H in HFPE52.



(a)



(b)

Figure 10: (a) Comparison of uniaxial stress strain responses of CG-PMR15 and CG-HFPE52 at a strain rate of $5 \times 10^8 \text{ s}^{-1}$ and temperature of 561 K and crosslink density $\chi = 0.8$. (b) Variation of the stress strain response of CG-PMR15 with crosslink density demonstrating that the steepening of the hardening response after yield is due to the fact that loss of crosslinks is not allowed in the simulation.

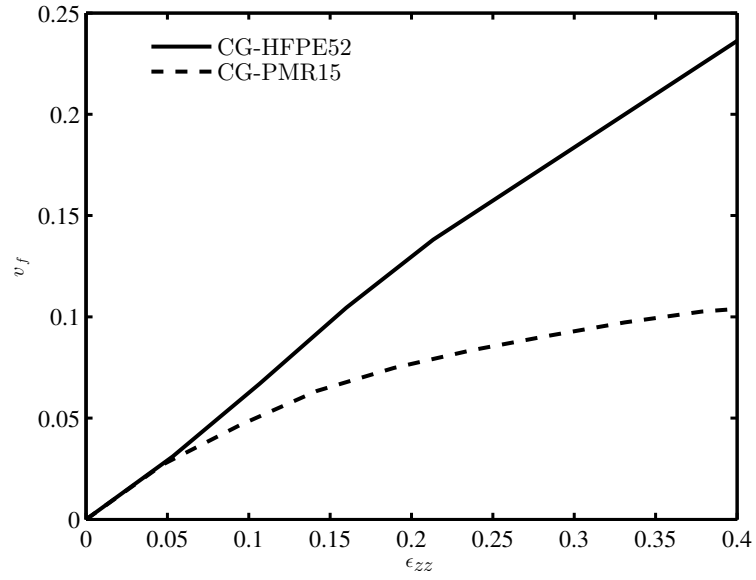


Figure 11: Evolution of void volume fraction with strain ϵ_{zz} in CG-PMR15 and CG-HFPE52.

A Optimised bond lengths, angles and dihedrals of PMR15

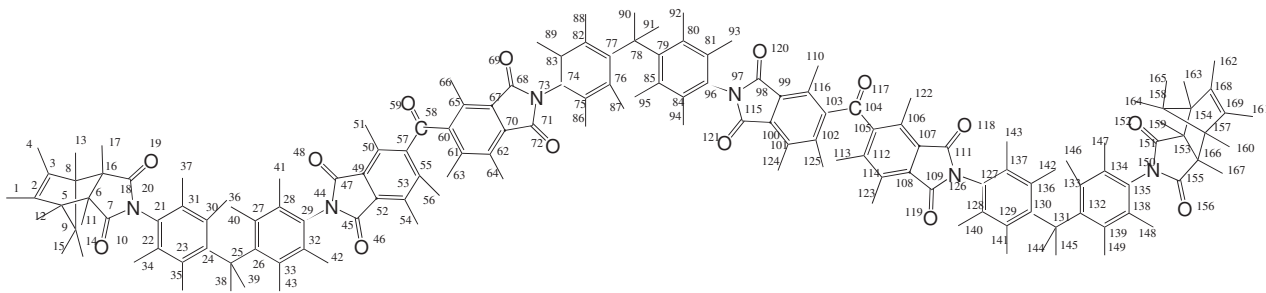


Figure A.1: The numbering of atoms in the all atom PMR15 molecule that has been used in this work. All subsequent data presented are based on this numbering scheme.

Atom pairs	Bond lengths from <i>ab-initio</i> calculations in Å
3 - 2	1.33
2 - 5	1.51
5 - 9	1.53
5 - 6	1.56
6 - 16	1.54
7 - 6	1.51
18 - 20	1.38
18 - 19	1.20
20 - 21	1.43
21 - 22	1.40
24 - 25	1.52
29 - 44	1.43
57 - 58	1.50
58 - 59	1.22

Table A.1: Distinct bond lengths for optimised PMR15. The numbering of atoms is according to Fig.A.1.

Connected atoms	Equilibrium values of bond angles from <i>ab-initio</i> cal- culations (in degrees)
2 - 3 - 8	107.58
3 - 8 - 9	100.17
2 - 5 - 6	99
5 - 9 - 8	94.58
9 - 5 - 6	99
5 - 6 - 16	103.14
6 - 16 - 18	105.20
16 - 18 - 20	107.16
7 - 20 - 18	115.25
16 - 18 - 19	128
20 - 21 - 22	120
18 - 20 - 21	122.39
21 - 22 - 23	120
30 - 24 - 25	120
24 - 25 - 26	114
29 - 44 - 45	124.28
44 - 45 - 46	126.11
44 - 45 - 52	105.74
45 - 52 - 49	108.45
49 - 50 - 57	117.73
49 - 52 - 53	121.58
50 - 57 - 55	120.23
57 - 58 - 60	120.77
57 - 58 - 59	119.62

Table A.2: Distinct bond angles for optimised PMR15. The numbering of atoms is according to Fig. A.1.

Connected atoms	Equilibrium values of dihedral angles in degrees from <i>ab-initio</i> calculations
2 - 3 - 8 - 9	33.20
3 - 8 - 9 - 5	50
2 - 5 - 6 - 7	179.6
2 - 5 - 6 - 16	66.6
9 - 5 - 6 - 16	37
5 - 6 - 7 - 20	113.83
5 - 6 - 7 - 10	-66.8
6 - 16 - 18 - 19	179.3
19 - 18 - 20 - 7	179.6
21 - 22 - 23 - 24	0
31 - 30 - 24 - 25	0
27 - 28 - 29 - 44	178.6
44 - 45 - 52 - 53	0.6
49 - 50 - 57 - 55	1.2
46 - 45 - 52 - 53	1.5
50 - 57 - 58 - 59	-27.24
55 - 57 - 58 - 59	148.58

Table A.3: distinct dihedral angles for optimised PMR15. The numbering of atoms is according to Fig. A.1

References

- [1] Rottler, J. and Robbins, M. O. 2001. Yield conditions for deformation of amorphous polymer glasses *Physical Review E*, **64**(5), 051801.
- [2] Rottler, J. and Robbins, M. O. 2003. Shear yielding of amorphous glassy solids: Effect of temperature and strain rate. *Physical Review E*, **68**(1), 011507.
- [3] Rottler, J. 2009. Fracture in glassy polymers: a molecular modeling perspective. *Journal of Physics: Condensed Matter*, **21**(46).
- [4] Vorselaars, B., Lyulin, A.V. and Michels, M.A.J. 2009. Microscopic mechanisms of strain hardening in glassy polymers. *Macromolecules*, **42**(15), 5829-5842.
- [5] Vorselaars, B., Lyulin, A.V. and Michels, M.A.J. 2009. Deforming glassy polystyrene : Influence of pressure, thermal history, and deformation mode on yielding and hardening. *Journal of Chemical Physics*, **130**(7), 074905.
- [6] Venkatesan, S. and Basu, S. 2014. Investigations into the origins of plastic flow and strain hardening in amorphous glassy polymers. *International Journal of Plasticity*, **56**, 139-155.
- [7] Mahajan, D. K., Estevez, R. and Basu, S. 2010. Ageing and rejuvenation in glassy amorphous polymers. *Journal of Mechanics and Physics of Solids*, **58**(10), 1474-1488.
- [8] Nouri, N and Ziaei-Rad, S. A Molecular Dynamics Investigation on Mechanical Properties of Cross-Linked Polymer Networks. *Macromolecules*, **44** (13), 54815489.
- [9] Zhang, Z., Zhang, L., Jasa, J., Li, W., Gazonas, G. and Negahban, M. 2017. High Fidelity Computational Characterization of the Mechanical Response of Thermally Aged Polycarbonate., *Modelling and Simulation in Materials Science and Engineering*, in press, <https://doi.org/10.1088/1361-651X/aa7341>.

- [10] Wilson, D., 1988. PMR-15 processing, properties and problems review. *British Polymer Journal*. **20**, 40596416.
- [11] Ando, S., 2004. Optical Properties of Fluorinated Polyimides and Their Applications to Optical Components and Waveguide Circuits. *Journal of Photopolymer Science and Technology*. **17(2)**.
- [12] Fraizer, B., 1995. Recent applications of polyimide to micromachining technology. *IEEE Transactions on Industrial Electronics*. **42(5)**.
- [13] Nazarychev, V. M., Lyulin, A. V., Larin, S. V., Gofman, I. V., Kenny, J. M. and Lyulin, S. V., 2016. Correlation between the High-Temperature Local Mobility of Heterocyclic Polyimides and Their Mechanical Properties, *Macromolecules*. **49**, 6700-10.
- [14] Lyulin, S. V., Larin, S. V., Gurtovenko, A. A., Nazarychev, V. M., Falkovich, S. G., Yudin, V. E., Svetlichnyi, V. M., Gofman, I. V. and Lyulin, A. V., 2016, *Soft Matter*, **10**, 1224-1232.
- [15] Majumder, M.K., Ramkumar, S., Mahajan, K., Basu, S., 2010. Coarse-graining scheme for simulating uniaxial stress-strain response of glassy polymers through molecular dynamics. *Physical Review E*. **81**, 011803.
- [16] Rosch, T.W., Brennan, J.K., Izvekov, S., Andzelm, J.W., 2013. Exploring the ability of a multiscale coarse-grained potential to describe the stress-strain response of glassy polystyrene. *Phys Rev E Stat Nonlin Soft Matter Phys*. **87(4)**, 042606.
- [17] Gaussian 09, Revision B.01, M. J. Frisch, G. W. Trucks, H. B. Schlegel, G. E. Scuseria, M. A. Robb, J. R. Cheeseman, G. Scalmani, V. Barone, B. Mennucci, G. A. Petersson, H. Nakatsuji, M. Caricato, X. Li, H. P. Hratchian, A. F. Izmaylov, J. Bloino, G. Zheng, J. L. Sonnenberg, M. Hada, M. Ehara, K. Toyota, R. Fukuda, J. Hasegawa, M. Ishida, T. Nakajima, Y. Honda, O. Kitao, H. Nakai, T. Vreven, J. A. Montgomery, Jr., J. E. Peralta, F. Ogliaro, M. Bearpark, J. J. Heyd, E. Brothers, K. N. Kudin, V. N. Staroverov, T. Keith, R. Kobayashi, J. Normand, K. Raghavachari, A. Rendell, J. C. Burant, S. S. Iyengar, J. Tomasi, M. Cossi, N. Rega, J. M. Millam, M. Klene, J. E. Knox, J. B. Cross, V. Bakken, C. Adamo, J. Jaramillo, R.

Gomperts, R. E. Stratmann, O. Yazyev, A. J. Austin, R. Cammi, C. Pomelli, J. W. Ochterski, R. L. Martin, K. Morokuma, V. G. Zakrzewski, G. A. Voth, P. Salvador, J. J. Dannenberg, S. Dapprich, A. D. Daniels, O. Farkas, J. B. Foresman, J. V. Ortiz, J. Cioslowski, and D. J. Fox, Gaussian, Inc., Wallingford CT, 2010.

- [18] Lee, C., Yang, W., Parr, R. G. 1988, Development of the Colle-Salvetti correlation-energy formula into a functional of the electron density. *Phys. Rev. B*, **37**, 785789.
- [19] Becke, A. D. 1993. Density-functional thermochemistry. III. The role of exact exchange. *J. Chem. Phys.*, **98**, 56485652.
- [20] Meador, B., Johnston, J. C., and Cavano, P.J., 1997. Elucidation of the Cross-Link Structure of Nadic-End-Capped Polyimides Using NMR of ¹³C-Labeled Polymers. *Macromolecules*. **30**, 515-519.
- [21] Odegard, G., and Kumosa, M., 2000. Elastic-plastic and failure properties of a unidirectional carbon/PMR-15 composite at room and elevated temperatures. *Composites Science and Technology*. **60(16)**, 2979-2988.
- [22] Farouk, A. and Langrana, N.A., 1992. Fracture properties of PMR-15/graphite-fiber composites. *Composites Science and Technology*. **45(3)**, 265-277.
- [23] McClung, A. J. W., (2008) Extension of viscoplasticity based on overstress to capture the effects of prior aging on the time dependent deformation of a high-temperature polymer: Experiments and modeling, Ph.D Thesis, Department of Aeronautics and Astronautics, Air Force Institute of Technology, Wright Patterson Air Force Base, Ohio.
- [24] Özmen Ö, (2009) Effects of Prior Aging at 316 C in Argon on Inelastic Deformation Behavior of PMR-15 Polymer at 316 C : Experiment and Modeling Thesis Air Force Institute of Technology, Wright-Patterson Air Force Base, Ohio.

- [25] Lai, J., and van der Giessen, E. (1997). A numerical study of crack-tip plasticity in glassy polymers, *Mechanics of Materials*, **25**, 183-197.
- [26] E. Krempl, Unified Constitutive Laws of Plastic Deformation. San Diego: Academic Press, 1996.
- [27] Tschop, W., Kremer, K., Batoulis, J., Burger, T., Hahn, O., (1998). Simulation of polymer melts. I. Coarse-graining procedure of polycarbonates. *Acta Polymer*. **49**, 61-74.
- [28] Akkermans, R. L. C., Briels, W. J., 2001. A structure-based coarse-grained model for polymer melts. *Journal of chemical physics*. **114**, 1020-1031.
- [29] Baschnagel, J., Binder, K., Doruker, P., Gusev, A. A., Hahn, O., Kremer, Kurt, Mattice, W. L., Muller-Plathe, F., Murat, M., Paul, W., Santos, S., Suter, U. W., Tries, V., 2000. Bridging the Gap Between Atomistic and Coarse-Grained Models of Polymers: Status and Perspectives. *Advances in Polymer Science*. **152**, 41-156.
- [30] Muller-Plathe, F., 2002. Coarse-Graining in Polymer Simulation: From the Atomistic to the Mesoscopic Scale and Back. *ChemPhysChem*. **3**, 754-769.
- [31] Sun, Q., Faller, R., (2005). Systematic coarse-graining of atomistic models for simulation of polymeric systems. *Computers and Chemical Engineering*. **29**, 2380-2385.
- [32] Izvekov, S., Voth, G. A., 2005. A Multiscale Coarse-Graining Method for Biomolecular systems. *Journal of physical chemistry letters B*. **109**, 2469-2473.
- [33] Chakravarty, A., and Cagin, T., 2010. Coarse grain modeling of polyimide copolymers. *Polymer* **51**, 2786-2794.
- [34] Sun, Q. and Faller, R., 2006. Systematic coarse-graining of a polymer blend: Polyisoprene and Polystyrene. *Journal of Chemical Theory and Computation*. **2(3)**, 607-615.

- [35] Depa, P. K., Maranas, J. K., 2005. Speed up of dynamic observables in coarse grained molecular-dynamics simulations of unentangled polymers. *The Journal of Chemical Physics*. **123**, 094901.
- [36] Plimpton, S.J., (1995). Fast Parallel Algorithms for Short-Range Molecular Dynamics. *Journal of Computational Physics*. **117**, 1-19.
- [37] Chuang, K. C., Bowman, C. L., Tsotsis, T. K., Arendt, C. P., (2003). 6F-Polyimides with Phenylethynyl Endcap for 315370 C Applications. *High Perform. Polym.* **15**, 459 - 472.
- [38] Pandiyan, S., Parandekar, P. V., Prakash, Om., Tsotsis, T. K. and Basu, S., (2015). Systematic Coarse Graining of a High-Performance Polyimide. *Macromolecular Theory and Simulations*. **24**, 513 - 520.
- [39] Jatin, Sudarkodi V, and Basu, S. (2014), Investigations into the origins of plastic flow and strain hardening in amorphous glassy polymers. *International Journal of Plasticity*. **56**, 139-155.
- [40] Xu, Y., Bhargava, P., and Zehnder, A., (2016). Time and temperature dependent mechanical behavior of HFPE-II-52 polyimide at high temperature. *Mechanics of Materials*. **100**, 86 - 95.
- [41] Ho, K., and Krempl, E., (2002). Extension of the viscoplasticity theory based on overstress (VBO) to capture non-standard rate dependence in solids. *International Journal of Plasticity*. **18**, 851 - 872.